Role of melting and solidification in the spreading of an impacting water drop

Wladimir Sarlin, Rodolphe Grivet, Julien Xu, Axel Huerre, Thomas Séon, Christophe Josserand

Role of melting and solidification in the spreading of an impacting water drop

Wladimir Sarlin[1] †, Rodolphe Grivet[1], Julien Xu[1], Axel Huerre[2], Thomas Séon[3], and Christophe Josserand[1] ‡

[1]Laboratoire d'Hydrodynamique, CNRS, École polytechnique, Institut Polytechnique de Paris, 91120 Palaiseau, France

[2]Laboratoire Matière et Systèmes Complexes (MSC), UMR CNRS 7057, Université Paris Cité, 75013 Paris, France

[3]Institut Franco-Argentin de Dynamique des Fluides pour l'Environnement (IFADyFE), IRL 2027, CNRS, UBA, CONICET, Buenos Aires, Argentine

(Received xx; revised xx; accepted xx)

The present study reports experiments of water droplet impacting on ice or on a cold metallic substrate, with the aim of understanding the effect of phase change on the impingement process. Both liquid and substrate temperatures are varied, as well as the height of fall. The dimensionless maximum spreading diameter, β_m, is found to increase with both temperatures as well as with the impact velocity. Furthermore, β_m is reduced when solidification, which enhances dissipation, is present, whereas fusion favours the liquid film spreading. These observations are rationalized by extending an existing model of effective viscosity, in which phase change alters the size and shape of the developing viscous boundary layer, thereby modifying the value of β_m. The use of this correction allows to adapt a scaling law existing for isothermal drop impacts to propose a universal law giving the maximum diameter of an impacting water droplet in the presence of melting or solidification.

Key words:

1. Introduction

In his poem *De Rerum Natura*, Lucretius asks: "*don't you see, besides, how drops of water falling down against the stones at last bore through the stones?*". This sentence, dating back to the first-century BC, is a testament to the long research interest for the problem of drop impacts on a substrate, which is always of topicality nowadays (Josserand & Thoroddsen 2016; Cheng *et al.* 2022). A better understanding of the droplet dynamics and maximum spreading diameter after impact is motivated by the wide range of industrial and natural applications such as, amongst others, spray deposition (Pasandideh-Fard *et al.* 2002), aeorosol

† Email address for correspondence: wladimir.sarlin@outlook.com
‡ Email address for correspondence: christophe.josserand@ladhyx.polytechnique.fr

generation (Joung & Buie 2015), or raindrop erosion (Zhao *et al.* 2015). In the isothermal situation, this led to the elaboration of models describing drop impacts in the capillary and viscous limits (Eggers *et al.* 2010), or in the transition between these two asymptotic regimes (Laan *et al.* 2014; Lee *et al.* 2016).

The particular configuration of drop impact involving phase change has also received a growing attention recently (Jin *et al.* 2017; Schremb *et al.* 2018; Ju *et al.* 2019; Thiévenaz *et al.* 2019; Gielen *et al.* 2020; Thiévenaz *et al.* 2020; Lolla *et al.* 2022; Grivet *et al.* 2023), due to its relevance for three-dimensional printing (Wang *et al.* 2016) or aircraft icing problematics (Baumert *et al.* 2018), for instance. If most of these studies focused on the sole case of solidification during a drop impact (Schremb *et al.* 2018; Gielen *et al.* 2020; Thiévenaz *et al.* 2020), few experimental works investigated the thermodynamic configuration in which the droplet is able to melt the solid surface it impacts (Jin *et al.* 2017; Ju *et al.* 2019; Lolla *et al.* 2022). However, so far a unified description of the influence of phase change on the maximum spreading diameter resulting from a drop impact remains elusive. These aspects motivated the present experimental study, which aims at investigating the case of a temperature-controlled water droplet falling onto a cold substrate, made either of ice or of cold brass, in order to understand the effects of melting and solidification on the impact outcome.

2. Experimental set-up and methods

The experimental set-up designed to this end is schematized in Figure 1(a). It consists of a 2.2 m high vertical beam, that holds an aluminium block which can be set at an adjustable height. A vertical needle of inner diameter 1.55 mm passes through the block, which was hollowed out to host a heating cartridge placed in contact with the needle and connected to a generator. At the bottom of the beam, a cooling unit can be used as is, or to generate an ice layer: it is made of a thin brass plate, cooled by a Peltier heat sink which is in turn connected to a cold bath operating with a mixture of water and ethylene glycol. Drop impacts can then be made directly onto cold enough brass, to study the role of solidification, or onto an ice layer, which is produced by depositing a certain amount of water on the plate before freezing it rapidly with the help of the Peltier modulus. When conducting experiments with the brass substrate, a perspex plate is placed on top of it to limit the formation of frost, without altering much its surface temperature due to the low thermal effusivity of plastic. This protection is removed just before performing a drop impact. A thermocouple, placed on top of the substrate, allows to adjust the heat flux imposed by the Peltier so that the brass or ice layer is set at an initial surface temperature T_s. At the beginning of an experiment, the needle temperature is monitored using a computer-controlled tension generator connected to the heating cartridge and to two thermocouples, respectively placed inside the needle and close to the cartridge. The needle is positioned so that its tip is located at a distance H from the substrate (with a 4 mm accuracy). Then, water is gently pushed into the needle using a syringe pump, and a pendant drop is formed. The drop eventually detaches from the needle with a controlled temperature T_d, measured with a ± 2 ℃ accuracy. Therefore, during the experiment, a water droplet of initial diameter D_0 starts its fall over the vertical distance H before impacting and spreading over the ice or brass substrate. This process is recorded from above by a high-speed camera, which operates at 5000 fps.

In the present study, the water droplet temperature T_d has been varied between 18 ℃ and 80 ℃, and the substrate temperature T_s between -33 ℃ and -2 ℃. The height H has been explored in the range $[0.04 - 2.2]$ m. The resultant impact velocity U of the water droplet is evaluated by a home-made code accounting for the air resistance, and varies here between 0.9 m.s^{-1} and 5.9 m.s^{-1}. For each initial condition, experiments are repeated three times to ensure reproducibility. Using standard correlations for the convective heat transfer of a sphere

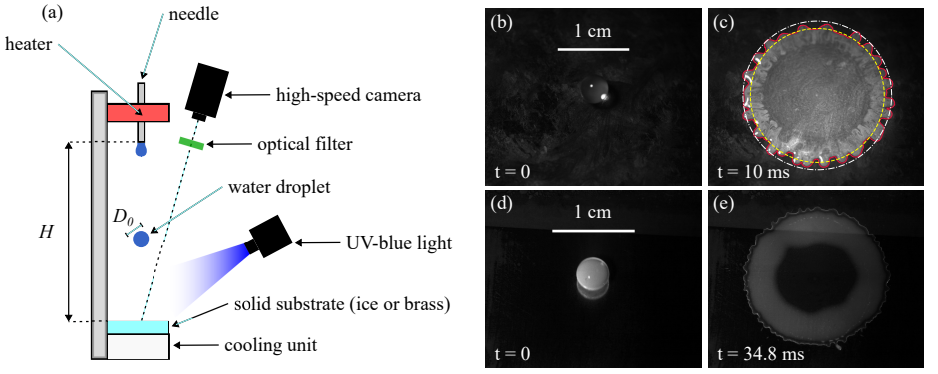

Figure 1: (a) Schematic representation of the experimental set-up. The initial diameter of the water drop is D_0, and the distance between its original position and the substrate is H. (b)-(c) Photographs of a transparent water droplet spreading on melting tinted ice, with $T_s = -5$ °C, $T_d = 25$ °C, and $H = 0.4$ m, at times (b) $t = 0$ and (c) $t = 10$ ms after the impact. (d)-(e) Pictures of a tinted water droplet spreading on cold brass, with $T_s = -32.2$ °C, $T_d = 19.3$ °C, and $H = 1.5$ m, at times (d) $t = 0$ and (e) $t = 34.8$ ms after the impact. Melting and solidification are evidenced here by the increase or decrease of the brightness with time, respectively, which reveals that more and more ice melts (resp., an increasing amount of water solidifies). In (c), the red line is the extracted contour of the liquid film when it reaches its maximum radial extent. Circles of diameter $D_{\min}$ (yellow dashed line) and $D_{\max}$ (white dash-dotted line) are also represented.

moving in a fluid (Yuge 1960; Pátek *et al.* 2009), the maximum temperature drop during the droplet's fall can be estimated to be less than 2 °C at worst (*i.e.*, when $T_d = 80$ °C and $H = 2.2$ m). As a result, we neglect this effect so that the droplet temperature at the time of impact is considered to be equal to T_d. Finally, the initial droplet diameter has been measured for all experiments from the last image showing the drop before the collision with the substrate. A slight effect of the water temperature T_d is observed, which is expected as different droplet temperatures result in different liquid surface tensions, hence to a modification of the volume of the initial pendant drop. Therefore, for a given water temperature T_d, the initial diameter D_0 is averaged over all experiments performed at that temperature.

3. Qualitative and quantitative results

When a water droplet impacts the substrate, it starts spreading radially on top of it. This expansion happens on the characteristic kinetic timescale D_0/U, of the order of milliseconds in the present experiments, until the drop reaches its maximum spreading diameter. After this moment, there is no significant retraction of the contact line on the substrate.

An important aspect is to determine whether the ice effectively melts, or the water solidifies, when the hot droplet impacts the substrate. To this end, two kinds of experiments are performed, where either the solid or liquid phase is dyed with fluorescein. The spreading is illuminated from above using a UV-blue light (with a wavelength of 470 nm), and the camera lens is covered by a green optical filter (with cutting wavelength of 495 nm), so that only fluorescent regions appear bright on the obtained images. In the first situation, the ice is dyed during its formation, whereas the impinging drop remains translucent. As fluorescence does not happen when fluorescein molecules are diluted in solid water, due to a self quenching phenomenon (Huerre *et al.* 2021), its detection is a signature of melted water originating from the ice layer. The pictures in Figure 1(b)-(c) show a view of the drop prior to the collision with the substrate and the final impact footprint when the maximum diameter has been attained, respectively, for a given initial configuration. If the initial droplet is almost not visible due to its transparency, the liquid phase becomes increasingly luminous as time goes

by: this demonstrates the melting of the ice during the whole impact process. Conversely, in the second case corresponding to a drop impact on cold brass, only the impinging liquid was dyed. The pictures in Figure 1(d)-(e) show a typical instance of this configuration, with the tinted droplet just before the first contact with the substrate (d) and the resulting imprint long after the spreading phase (e). The fact that the intensity in the liquid decreases with time, with some part of the impacted drop becoming completely dark, reveals that solidification of the liquid layer is at play. It should be mentioned that these phenomena are also visible during the expanding stage: it suggests that the two typical times of radial expansion and of phase change are of the same order, so that there is no scale separation between the two processes.

In order to study quantitatively the impact outcome, we performed drop impact experiments on ice or cold brass, in which water has been tinted with fluorescein and the parameters T_d, T_s, and H have been varied systematically in the ranges indicated in section 2. The final imprint contour, obtained when the liquid film reaches its maximum radial extent, can then be extracted as illustrated by the red solid line in Figure 1(c). Image processing allows to locate the positions of the local maxima (*i.e.*, the tip of the digitations) and minima (located between two fingers), relative to the center of mass of the contour (O). From the corresponding radial distances to O, the minimum and maximum diameters, noted respectively $D_{\min}$ and $D_{\max}$, are defined as the averaged positions of the local minima and maxima, respectively. From all our experiments, we observe a linear relationship between $D_{\max}$ with $D_{\min}$ regardless of the droplet or substrate temperatures, following $D_{\max} = 1.07 D_{\min}$. As a result, the more the spreading, the more the fingers' elongation. The proportionality between the two diameters is an intriguing result, which suggests that here the typical size of the digitation $D_{\max} - D_{\min}$ is about 7% of the spreading diameter $D_{\min}$, and that $D_{\max}$ can be described in a similar way as $D_{\min}$. As a result, the maximum spreading ratio is defined as $\beta_m \equiv D_{\min}/D_0$, with D_0 the initial diameter of the droplet.

In Figure 2, β_m is presented as a function of the impact velocity U, for a fixed droplet temperature T_d (a)-(c) or substrate temperature T_s (d)-(f), that are indicated above each plot. The markers correspond to experiments with (◊) solidification or (○) fusion, respectively. In all cases, the spreading ratio clearly increases with U. Furthermore, for a fixed value of T_d, increasing T_s results in larger β_m: the higher the substrate temperature, the larger the spreading ratio. This is illustrated for ice in (b) and (c) where $T_d = 50$ ℃ and $T_d = 80$ ℃, respectively: in these cases, experiments conducted at $T_s = -2$ ℃ (dark blue) are significantly above those performed at $T_s = -25$ ℃ (light blue). To a lesser extent, at a given value of T_s, β_m is larger when T_d is increased. This is especially visible in (f) for $T_s = -2$ ℃, where a gentle order exists with the value of the droplet temperature T_d. These observations agree with the results gathered by Jin *et al.* (2017) and Ju *et al.* (2019) for drop impacts on ice, and by Thiévenaz *et al.* (2020) for droplet impingements on a cold metal substrate.

4. Discussion and modelling

Except for a few data which have a small falling distance H, the impact velocities in the present experiments are large ($U \gtrsim 2$ m/s). The impact outcome is thus expected in these cases to be mainly dictated by an equilibrium between inertia and viscous dissipation (Laan *et al.* 2014), and hence our data to be well parametrised by the Reynolds number of the impact, which compares both phenomena. It is defined here as $\mathrm{Re} \equiv \mathrm{U}D_0/\nu_\mathrm{f}$, with ν_f the water kinematic viscosity evaluated at the melting point $T_f = 0$ ℃ using standard correlations (Pátek *et al.* 2009). The evolution of β_m with Re is illustrated in Figure 3(a). Overall, the spreading ratio is found to increase with the Reynolds number, however it can be noticed that the data are scattered in this representation. Indeed, a gentle order appears with T_s, which is

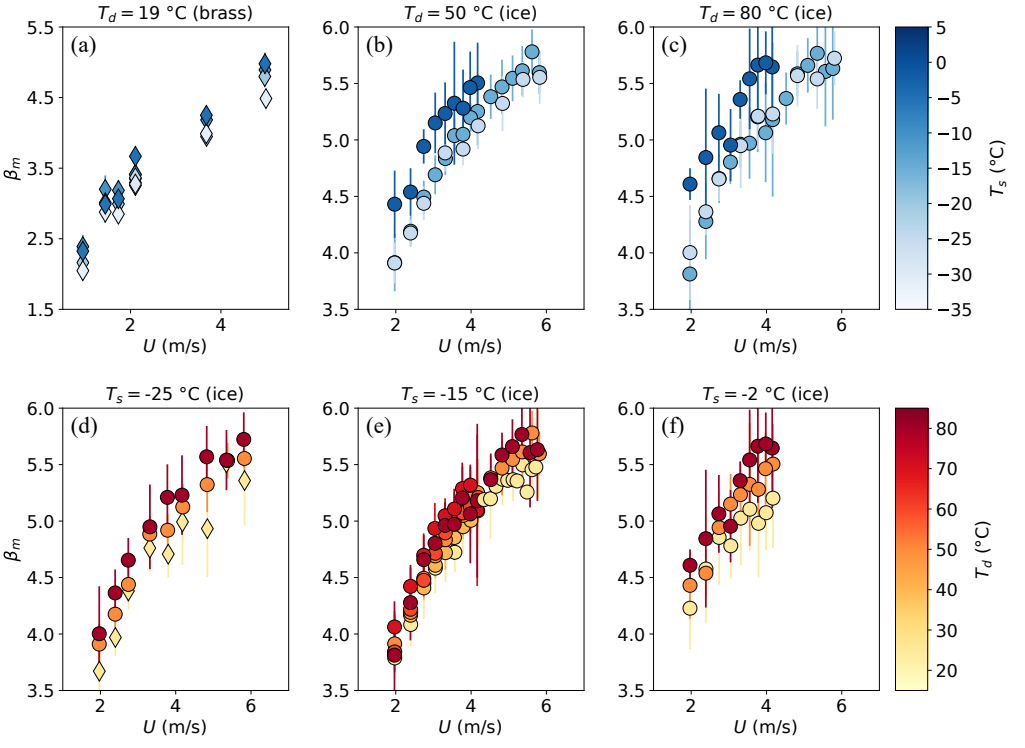

Figure 2: Evolution of the maximum spreading ratio $\beta_m \equiv D_{\min}/D_0$, as a function of the impact velocity U. In (a)-(c), the droplet temperature is fixed at (a) $T_d = 19$ °C, (b) $T_d = 50$ °C, and (c) $T_d = 80$ °C, while the colorbar denotes the substrate temperature T_s. Contrariwise, in (d)-(f) the substrate temperature is fixed at (d) $T_s = -25$ °C, (e) $T_s = -15$ °C, and (f) $T_s = -2$ °C, while the markers' colours represent this time the droplet temperature T_d. The symbols correspond to experiments with (◊) solidification or (○) fusion, respectively. The nature of the substrate is indicated above each plot.

visible for instance for the experiments in which ice melts (○), as illustrated by the inset of Figure 3(a). In addition, for a given Reynolds number, experiments featuring solidification (◊) have a systematically smaller value for β_m than data involving melting (○).

The poor collapse of the data in this representation is, in fact, expected as the spreading dynamics is affected by the presence of phase change (Thiévenaz *et al.* 2020). Indeed, in such a situation, the ice grows or melts at the base of the expanding liquid film, as illustrated in Figure 3(b)-(c), thus changing the position of the solid surface on which the viscous boundary layer of thickness δ_ν develops, thereby modifying the value of β_m. The position of the moving interface can, at first order, be modelled by the classical Stefan problem, if one assumes that the influence of advection is negligible. The importance of this latter effect is known to depend on the Prandtl number Pr, which compares the typical sizes of the thermal and viscous boundary layers (Roisman 2010; Moita *et al.* 2010). As in the case of water close to its melting point this number is quite high (Pr $\sim$ 14 at 0.01°C), it can be considered that the heat diffusion is marginally affected by the advection in the present experiments. We thereby solve the Stefan problem by taking into account heat diffusion both in the liquid and the solid phase, leading to the usual self-similar solution for the temperature field (Thiévenaz *et al.* 2019). To put it in a nutshell, under these assumptions the front of the ice layer h follows a diffusive law of the form $h(t) = s\sqrt{D_{\text{eff}}t}$, where $s = -1$ in the case of melting (resp., $s = 1$ for solidification), and D_{eff} is an effective thermal diffusion coefficient ($D_{\text{eff}} \geqslant 0$).

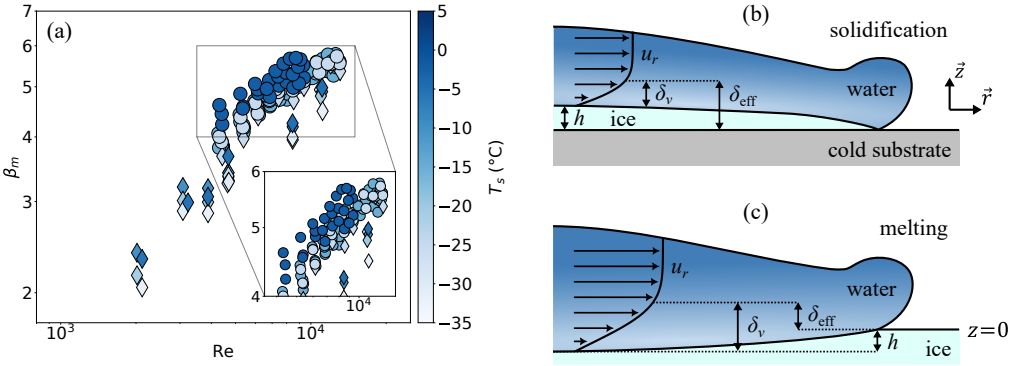

Figure 3: (a) Maximum spreading ratio β_m as a function of the Reynolds number, Re. The colorbar indicates the substrate temperature, while the symbols are the same as in Figure 2. (b)-(c) Schematic views of the ice (b) growth or (c) melting during the film spreading. δ_v corresponds to the size of the viscous boundary layer, h is the position of the substrate, and δ_{eff} the size of the effective boundary layer, whereas u_r is the radial velocity field.

By introducing $\alpha = s\sqrt{D_{\text{eff}}/D_i}$, with D_i the ice thermal diffusivity, D_{eff} and s are found numerically by solving the transcendental equation on α

$$\frac{\alpha\sqrt{\pi}}{2\text{St}} = \frac{e^{-\alpha^2/4}}{e_i/e_s + \text{erf}\,(\alpha/2)} + \frac{e_d}{e_i}\frac{e^{-\alpha^2/(4\omega)}}{1 - \text{erf}\,(\alpha/(2\sqrt{\omega}))}\frac{T_f - T_d}{T_f - T_s}, \tag{4.1}$$

with e_d, e_i and e_s the thermal effusivities of water, ice, and of the possible substrate, respectively ($e_s = e_i$ for drop impacts on ice), $\omega = D_d/D_i$ with D_d the water thermal diffusivity, and $\text{St} = c_p(T_f - T_s)/\mathcal{L}_f$ the Stefan number (with c_p the ice thermal capacity and $\mathcal{L}_f$ the latent heat of fusion for water). For each experiment, the obtained value for s reveals whether freezing ($s = 1$) or melting ($s = -1$) occurred, and the symbol used in Figures 2 and 3(a) are chosen accordingly.

From there, following the previous approaches developed by Eggers *et al.* (2010), Roisman (2010) and later by Thiévenaz *et al.* (2020), it is possible to estimate the size of the viscous boundary layer relative to the initial position of the substrate, which is expected to eventually dictate the arrest. This is done by considering the $r-$component of the axisymmetric Navier-Stokes equations using the Prandtl boundary layer framework for an incompressible flow:

$$\partial_t u_r + u_r\partial_r u_r + u_z\partial_z u_r = \nu_f\partial_z^2 u_r, \tag{4.2}$$

where u_r and u_z are the radial and vertical components of the velocity field, respectively, and ∂_a stands for partial differentiation with respect to variable a. Using the stream function ψ, defined from $u_r \equiv -\partial_z\psi/r$ and $u_z \equiv \partial_r\psi/r$, the inviscid solution describing the impact can be taken as $\psi = -r^2 z/t$ corresponding to a time decreasing arrest point flow: $u_r = r/t$ and $u_z = -2z/t$. Since both the viscous boundary layer, growing from the ice layer located at $z = h(t)$, and the melted or solidified ice layer $h(t)$ follow a $\sqrt{t}$ law, we can consider the following ansatz for the flow:

$$\psi \equiv \sqrt{\nu_f}\frac{r^2}{\sqrt{t}}f(\zeta), \tag{4.3}$$

where $\zeta = [z - h(t)]/\sqrt{\nu_f t}$ is the self-similar variable and f an unknown function of ζ. As $u_r = -(r/t)f'(\zeta)$, f' provides an insightful description of the shape of the boundary layer.

Following Thiévenaz *et al.* (2020), we inject the expression of ψ into equation (4.2), which leads to

$$f''' = -f' - \frac{1}{2}\left(\zeta + s\sqrt{\frac{D_{\text{eff}}}{\nu_f}}\right) f'' - f'^2 + 2ff''. \tag{4.4}$$

The boundary conditions are a zero velocity at the ice-water interface $\zeta = 0$, and the recovery of the inviscid profile at infinity: this translates into $f(0) = 0$, $f'(0) = 0$, and $f'(+\infty) = -1$, respectively. The resolution of equation (4.4) for these boundary conditions is achieved numerically, by using a shooting method algorithm. The evolution of ζ as a function of $-f'$ (*i.e.*, in a "velocity profile"-like representation) is illustrated in Figure 4(a), for several representative values of $\sigma \equiv s\sqrt{D_{\text{eff}}/\nu_f}$. For each case, $-f'$ increases from 0 at the contact with the substrate to 1 for $\zeta \simeq 2$, where the inviscid flow solution is thereby recovered. Furthermore, the curves for different values of σ depart from each other, with those having high values of this parameter reaching the asymptotic behaviour earlier, meaning that the viscous boundary layer in this case is reduced in size when compared to lower σ. Therefore, this suggests that the typical form factor of the viscous boundary layer, that can roughly be estimated as $\xi \simeq -1/f''(0)$, is a function of σ. In other terms, the present modelling predict a coupling between the flow and the phase change dynamics. This fact can be verified in Figure 4(b), where ξ decreases with σ in a weakly non-linear manner. In the present experiments, ξ ranges from 0.86 (for $\sigma \simeq 0.35$) to 1.04 (for $\sigma \simeq -0.2$). These values are highlighted in Figure 4(b) by the dash-dotted and dashed lines, respectively.

It then becomes possible to evaluate the vertical height δ_{eff} reached by the viscous boundary layer compared to the initial substrate position from $\xi = [\delta_{\text{eff}} - h(t)]/\sqrt{\nu_f t}$. This yields

$$\delta_{\text{eff}} = \xi\sqrt{\nu_f t} + s\sqrt{D_{\text{eff}} t}. \tag{4.5}$$

Noticeably, this height displays a diffusive-like behaviour. Therefore, we introduce an effective water kinematic viscosity, ν_{eff}, which is defined as $\delta_{\text{eff}} \equiv \xi\sqrt{\nu_{\text{eff}} t}$, so that

$$\nu_{\text{eff}} = \left(\sqrt{\nu_f} + \frac{s}{\xi}\sqrt{D_{\text{eff}}}\right)^2. \tag{4.6}$$

In the case of solidification, one obtains $\nu_{\text{eff}} > \nu_f$, which means that the viscous boundary layer will reach the liquid free-surface sooner than for an isothermal drop impact. Freezing thus enhances dissipation, and reduces the spreading diameter. Conversely, for fusion $\nu_{\text{eff}} < \nu_f$: the boundary layer will meet the free-surface later than for the isothermal case, so that dissipation is reduced while spreading is favoured by substrate melting. For some experiments, the effective kinematic viscosity that is predicted differs significantly from ν_f: for instance, for drop impacts on ice where $T_s = -2$ °C and $T_d = 80$ °C, one obtains $\nu_{\text{eff}} \simeq 0.65\nu_f$. We stress out that, in this model, the two cases of solidification and melting during the impact of a water drop onto its solid phase are encompassed into the same framework, which generalizes the approach followed by Thiévenaz *et al.* (2020).

As a result of this analysis, we define an effective Reynolds number as $\text{Re}_{\text{eff}} \equiv \text{UD}_0/\nu_{\text{eff}}$, *i.e.*, based on the effective viscosity ν_{eff} which is evaluated using equation (4.6). Thus, Re_{eff} takes into account the influence of phase change on the development of the viscous boundary layer. The spreading ratio β_m is shown as function of Re_{eff} in Figure 4(c). This representation reveals a collapse of all our experimental data onto a master curve, regardless of the nature of the initial substrate (brass or ice) and the dynamics of the ice-water interface (melting or solidification). This shows that the effective Reynolds number captures the physics at play,

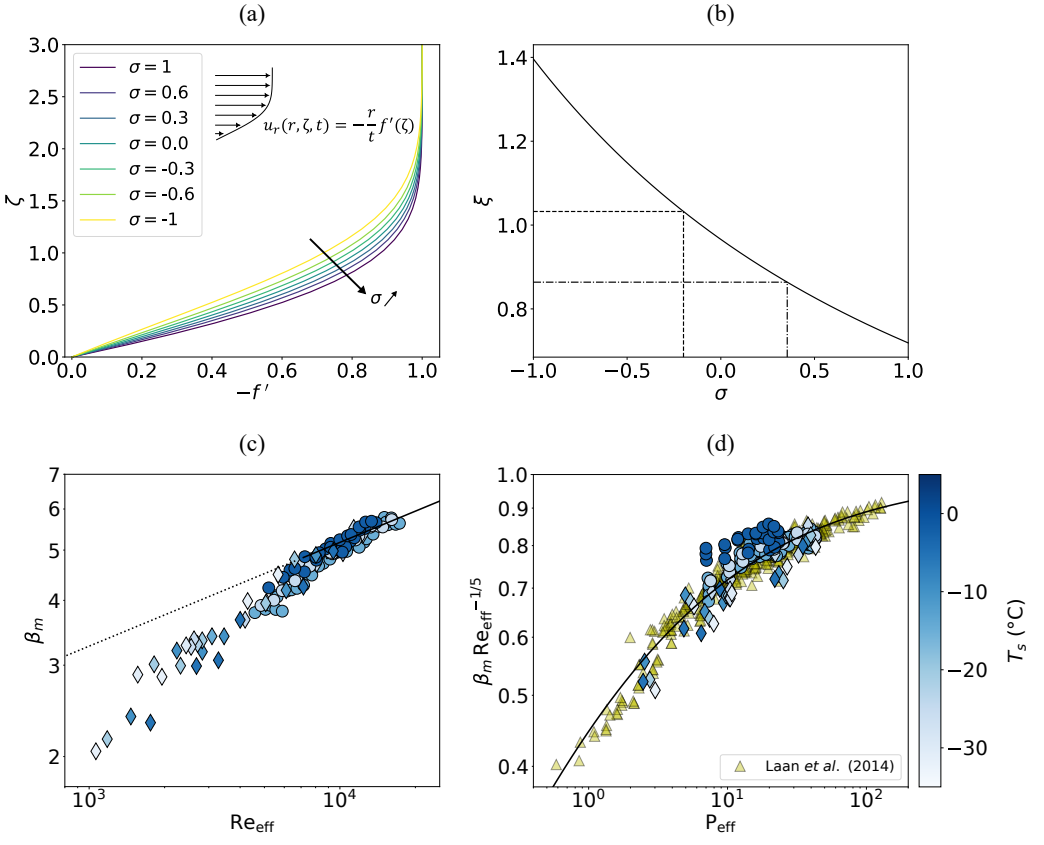

Figure 4: (a) Evolution of the self-similar variable $\zeta = [z - h(t)]/\sqrt{\nu_f t}$ as a function of $-f'$ ("velocity profile" representation). Each curve correspond to a given value of $\sigma \equiv s\sqrt{D_{\mathrm{eff}}/\nu_f}$. (b) Evolution of the form factor $\xi = -1/f''(0)$ of the viscous boundary layer as a function of σ. The dashed and dash-dotted lines highlight the ranges covered in the present experiments. (c) Evolution of β_m with the effective Reynolds number $\mathrm{Re_{eff}} \equiv \mathrm{UD_0}/\nu_{\mathrm{eff}}$, with ν_{eff} the effective kinematic viscosity defined in equation (4.6). The line indicates $\beta_m = 0.82\,\mathrm{Re_{eff}}^{1/5}$. (d) $\beta_m \mathrm{Re_{eff}}^{-1/5}$ as a function of the impact parameter $\mathrm{P_{eff}} \equiv \mathrm{We_{eff}Re_{eff}}^{-2/5}$. The data (△) as well as the universal law (solid black line) obtained by Laan *et al.* (2014) for isothermal drop impacts are also reported. The colorbar indicates the substrate temperature, while the symbols are the same as in figure 2.

contrary to the Reynolds number [see Figure 3(a)]. Furthermore, data located at large $\mathrm{Re_{eff}}$ ($\mathrm{Re_{eff}} \gtrsim 7 \times 10^3$) are compatible with the usual viscous-inertial scaling $\beta_m \propto \mathrm{Re_{eff}}^{1/5}$, as illustrated by the solid line reported in Figure 4(c). Nevertheless, data at lower values of $\mathrm{R_{eff}}$ significantly depart from the $1/5$ power law, and also appear to be slightly more scattered. Such a behaviour is reminiscent of the transition from the inertial-viscous regime to the inertial-capillary regime, which has been thoroughly discussed in previous studies (Laan *et al.* 2014; Lee *et al.* 2016). In the capillary limit, the initial kinetic energy of the drop, which scales as $\rho U^2 {D_0}^3$, is completely converted into surface energy which scales as $\gamma {D_{\mathrm{min}}}^2$ (with ρ and γ the density and surface tension of the drop, respectively). As a result, one obtains the scaling $\beta_m \sim \mathrm{We}^{1/2}$, with $\mathrm{We} \equiv \rho \mathrm{U}^2 \mathrm{D_0}/\gamma$ the Weber number (Eggers *et al.* 2010). Contrariwise, in the viscous regime, the kinetic energy is balanced by viscous dissipation, which leads to the scaling $\beta_m \sim \mathrm{Re}^{1/5}$ (Eggers *et al.* 2010). To bridge

between these two asymptotic scenarii, a universal rescaling has been proposed by Laan *et al.* (2014) in the context of isothermal drop impacts, in which $\beta_m \mathrm{Re}^{-1/5}$ is a function of a sole impact parameters, $\mathrm{P} \equiv \mathrm{We}\,\mathrm{Re}^{-2/5}$. Adopting this approach, and using $\mathrm{Re_{eff}}$ instead of Re, we plot in Figure 4(d) the evolution of the rescaled spreading ratio $\beta_m \mathrm{Re_{eff}}^{-1/5}$ as a function of the impact parameter $\mathrm{P_{eff}} \equiv \mathrm{We}\,\mathrm{Re_{eff}}^{-2/5}$, for all our experiments. The values for ρ and γ, involved in the expression of We, are taken at T_d. In addition, the data from Laan *et al.* (2014) ($\triangle$) corresponding to isothermal drop impacts, are reported in Figure 4(d) with $\mathrm{Re_{eff}} = \mathrm{Re}$ and $\mathrm{P_{eff}} = \mathrm{P}$. Very noticeably, impacts involving solidification ($\Diamond$) as well as most experiments featuring fusion ($\bigcirc$) superimpose with the data of Laan *et al.* (2014), and are captured by the universal empirical law

$$\beta_m \mathrm{Re_{eff}}^{-1/5} = \frac{\sqrt{\mathrm{P_{eff}}}}{1.24 + \sqrt{\mathrm{P_{eff}}}}, \tag{4.7}$$

evidenced by these authors for the isothermal case (solid black line). The deviation of these experiments from equation (4.7) is less than 10%, similar to the dispersion of the original data from Laan *et al.* (2014). However, a closer inspection reveals that the impacts on an ice substrate at $T_s = -2$ ℃ (dark blue circles) slightly deviate from relation (4.7). As these experiments belong to the transition region ($\mathrm{P_{eff}} \sim 10$), and as their initial substrate temperature is close to the melting point, this suggests that wettability effects could start to have a significant influence here (Lee *et al.* 2016). Nevertheless, as the wetting of water on ice is still a subject of active research, it is not straightforward to conclude on that aspect within the present analysis.

5. Conclusion

In the present investigation, experiments of water drop impacts onto ice and cold brass were performed, in which both liquid and substrate temperatures were varied, alongside with the falling height, in order to reach a deeper understanding of the influence of melting and solidification on the impact process. The maximum spreading ratio is found to increase with both temperatures as well as with the impact velocity, and the typical size of the corrugations, when present, is proportional to the final radial extent of the liquid film. Phase change results in a modification of the viscous boundary layer, thereby affecting the overall viscous dissipation. Modelling this effect through the use of an effective viscosity allows to capture the physics at play, and to relate it to a universal law developed for the isothermal configuration. These results pave the way for a comparison with drop impacts of molten metal on cold substrate or in the presence of evaporation, which could further validate the approach followed here. Another situation of interest, for practical applications as well as to extend the results from the present work, would be to investigate the case of non-isothermal drop impacts in the absence of phase change. Indeed, in this scenario, varying the temperature of the initial droplet or the substrate is expected to change the value of the contact temperature, and thus to affect the behaviour of the thermal and viscous boundary layers, which should in turn modify the liquid film spreading.

Acknowledgements. The authors warmly thank Caroline Frot and Antoine Garcia for their help in the elaboration of the experimental set-up.

Funding. This work was partially supported by Agence de l'Innovation de Défense (AID) - via Centre Interdisciplinaire d'Etudes pour la Défense et la Sécurité (CIEDS) - (project 2021 - ICING).

Declaration of interests. The authors report no conflict of interest.

Author ORCIDs. W. Sarlin, https://orcid.org/0000-0002-2668-2279; R. Grivet, https://orcid.org/0000-0002-1489-7336; A. Huerre, https://orcid.org/0000-0003-4702-5128; T. Séon, https://orcid.org/0000-0001-6728-6072; C. Josserand, https://orcid.org/0000-0003-1429-4209

Author contributions. W. S. and R.G. contributed equally to the present study.

REFERENCES

Baumert, A., Bansmer, S., Trontin, P. & Villedieu, P. 2018 Experimental and numerical investigations on aircraft icing at mixed phase conditions. *Int. J. Heat Mass Transf.* **123**, 957–978.

Cheng, X., Sun, T.-P. & Gordillo, L. 2022 Drop impact dynamics: Impact force and stress distributions. *Annu. Rev. Fluid Mech.* **54** (1), 57–81.

Eggers, J., Fontelos, M. A., Josserand, C. & Zaleski, S. 2010 Drop dynamics after impact on a solid wall: Theory and simulations. *Phys. Fluids* **22** (6), 062101.

Gielen, M. V., Ruiter, R. de, Koldeweij, R. B. J., Lohse, D., Snoeijer, J. H. & Gelderblom, H. 2020 Solidification of liquid metal drops during impact. *J. Fluid Mech.* **883**, A32.

Grivet, R., Huerre, A., Séon, T. & Josserand, C. 2023 Making superhydrophobic splashes by surface cooling. *Phys. Rev. Fluids* **8**, 063603.

Huerre, A., Monier, A., Séon, T. & Josserand, C. 2021 Solidification of a rivulet: shape and temperature fields. *J. Fluid Mech.* **914**, A32.

Jin, Z., Zhang, H. & Yang, Z. 2017 Experimental investigation of the impact and freezing processes of a water droplet on an ice surface. *Int. J. Heat Mass Transf.* **109**, 716–724.

Josserand, C. & Thoroddsen, S. T. 2016 Drop impact on a solid surface. *Annu. Rev. Fluid Mech.* **48**, 365–391.

Joung, Y. S. & Buie, C. R. 2015 Aerosol generation by raindrop impact on soil. *Nat. Commun.* **6** (1), 6083.

Ju, J., Yang, Z., Yi, X. & Jin, Z. 2019 Experimental investigation of the impact and freezing processes of a hot water droplet on an ice surface. *Phys. Fluids* **31** (5), 057107.

Laan, N., de Bruin, K. G., Bartolo, D., Josserand, C. & Bonn, D. 2014 Maximum diameter of impacting liquid droplets. *Phys. Rev. Appl.* **2**, 044018.

Lee, J. B., Laan, N., de Bruin, K. G., Skantzaris, G., Shahidzadeh, N., Derome, D., Carmeliet, J. & Bonn, D. 2016 Universal rescaling of drop impact on smooth and rough surfaces. *J. Fluid Mech.* **786**, R4.

Lolla, V. Y., Ahmadi, S. F., Park, H., Fugaro, A. P. & Boreyko, J. B. 2022 Arrested dynamics of droplet spreading on ice. *Phys. Rev. Lett.* **129**, 074502.

Moita, A. S., Moreira, A. L. N. & Roisman, I. V. 2010 Heat transfer during drop impact onto a heated solid substrate. *14th Int. Heat Transf. Conf.* **6**, 803–810.

Pasandideh-Fard, M., Pershin, V., Chandra, S. & Mostaghimi, J. 2002 Splat shapes in a thermal spray coating process: simulations and experiments. *J. Therm. Spray Technol.* **11**, 206–217.

Pátek, J., Hrubý, J., Klomfar, J., Součková, M. & Harvey, A. H. 2009 Reference Correlations for Thermophysical Properties of Liquid Water at 0.1MPa. *J. Phys. Chem. Ref. Data* **38** (1), 21–29.

Roisman, I. V. 2010 Fast forced liquid film spreading on a substrate: flow, heat transfer and phase transition. *J. Fluid Mech.* **656**, 189–204.

Schremb, M., Roisman, I. V. & Tropea, C. 2018 Normal impact of supercooled water drops onto a smooth ice surface: experiments and modelling. *Journal of Fluid Mechanics* **835**, 1087–1107.

Thiévenaz, V., Séon, T. & Josserand, C. 2019 Solidification dynamics of an impacted drop. *J. Fluid Mech.* **874**, 756–773.

Thiévenaz, V., Séon, T. & Josserand, C. 2020 Freezing-damped impact of a water drop. *EPL* **132** (2), 24002.

Wang, C.-H., Tsai, H.-L., Wu, Y.-C. & Hwang, W.-S. 2016 Investigation of molten metal droplet deposition and solidification for 3d printing techniques. *J. Micromech. Microeng.* **26** (9), 095012.

Yuge, T. 1960 Experiments on heat transfer from spheres including combined natural and forced convection. *J. Heat Transf. (US)* **82**.

Zhao, R., Zhang, Q., Tjugito, H. & Cheng, X. 2015 Granular impact cratering by liquid drops: Understanding raindrop imprints through an analogy to asteroid strikes. *Proc. Natl. Acad. Sci. U.S.A.* **112** (2), 342–347.